

Electronic Supplementary Information

1. Fourier Transform Infrared spectroscopy (FT-IR) and Elemental Analyses for **1** and **2**.
2. Single-crystal X-Ray Diffraction (XRD) data for **CuNaph**.
3. Thermal desorption mass spectrometry (TD-MS) data for **2**.
4. Synchrotron Powder X-Ray Diffraction (PXRD) data for **1** and **2**.

1. FT-IR and Elemental Analyses for **1**, **2**, and **CuNaph**.

**1:**

Anal. Calcd for C<sub>56</sub> H<sub>48</sub> Cu<sub>5</sub> N<sub>8</sub> O<sub>16</sub>: C, 47.81; H, 3.44%. Found: C, 49.12; H, 4.32%. FT-IR (ATR, 4000-500 cm<sup>-1</sup>) 1623vs, 1605vs, 1561w, 1498w, 1424s, 1349w, 1222w, 1000m, 889w, 860w, 821w, 803m, 750w, 742w, 728w, 720w, 680vs, 663m, 628m, 579m, 564w, 557w, 529w, 523m, 517m, 513m, 509vs cm<sup>-1</sup>.

**2:**

Anal. Calcd for C<sub>128</sub> H<sub>80</sub> Cu<sub>5</sub> N<sub>8</sub> O<sub>16</sub>: C, 66.73; H, 3.50%. Found: C, 67.95; H, 3.74%. FT-IR (ATR, 4000-500 cm<sup>-1</sup>) 1625m, 1606vs, 1588s, 1507m, 1459w, 1417m, 1375s, 1257w, 1218w, 1151w, 1083w, 1072w, 1000m, 973w, 876w, 871w, 869w, 796s, 777vs, 759m, 743m, 715m, 681m, 659s, 580w, 566w, 562w, 539m, 512s cm<sup>-1</sup>.

**CuNaph • 2H<sub>2</sub>O:**

Anal. Calcd for C<sub>44</sub> H<sub>32</sub> Cu<sub>2</sub> O<sub>10</sub>: C, 62.33; H, 3.80%. Found: C, 61.92; H, 3.60%. FT-IR (ATR, 4000-500 cm<sup>-1</sup>) 1623w, 1600m, 1579m, 1562s, 1509m, 1458w, 1433w, 1402s, 1377s, 1357s, 1344s, 1253m, 1216w, 1153w, 1010w, 873w, 778vs, 762m, 742w, 660s, 620w, 590w, 576w, 542s, 524m, 515s, 509vs cm<sup>-1</sup>.

2. Single-crystal XRD data for **CuNaph • 2MeOH**.

**CuNaph** was synthesized by a ligand exchange method similar to that described in the literature,<sup>8</sup> and the structure was confirmed by single-crystal XRD analysis.

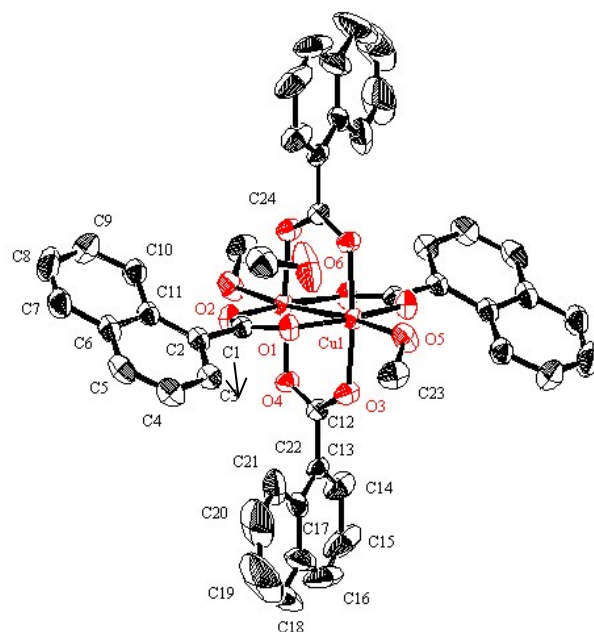


**Figure 1S-1.** (a) ORTEP view of **CuNaph • 2MeOH**. For clarity, H atoms have been omitted.

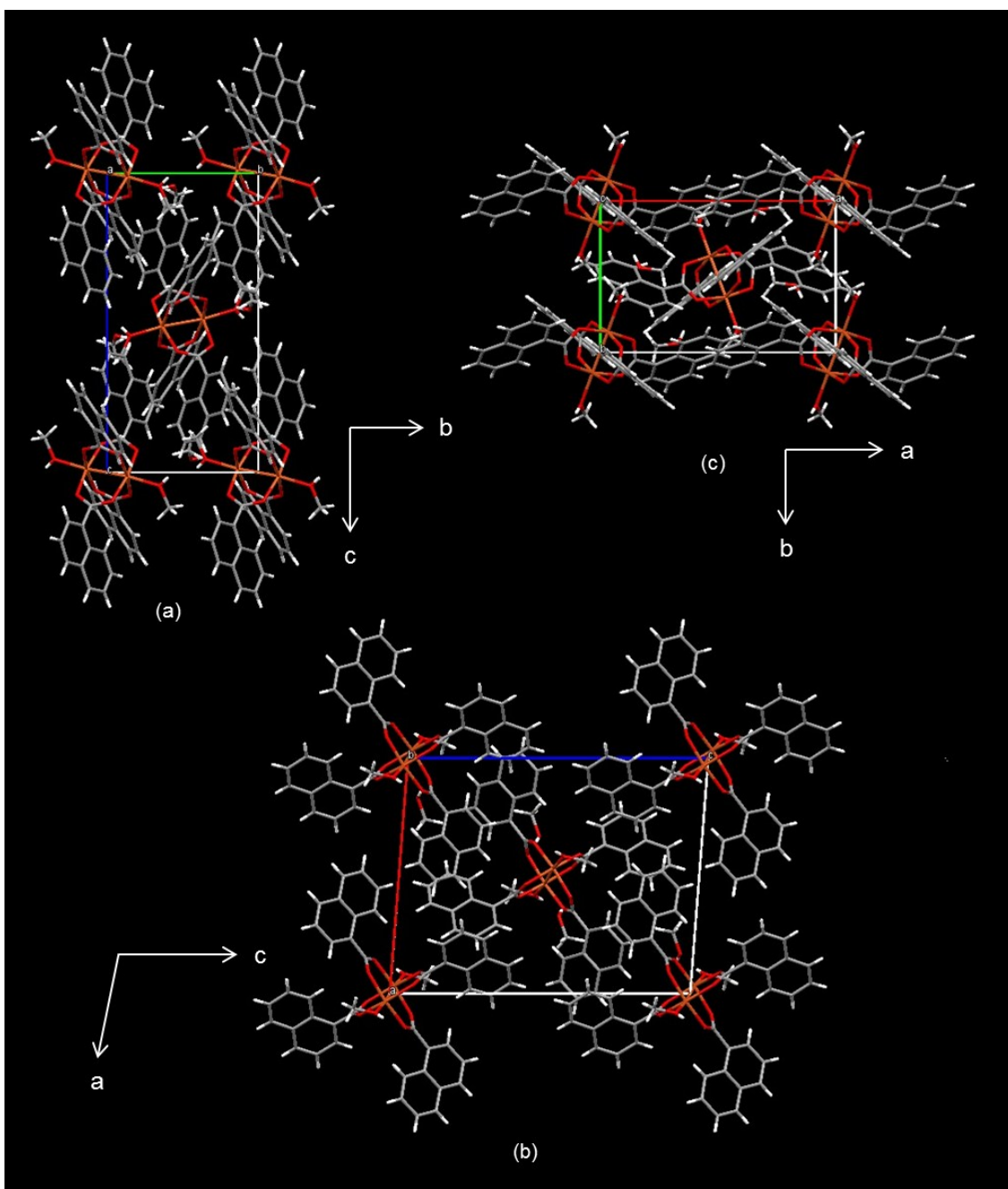


**Figure 1S-2.** Crystal packing of CuNaph·2MeOH along the (a) *a*-axis, (b) *b*-axis, and (c) *c*-axis.

### 3. TD-MS data for **2**.

To elucidate the stability of each of these frameworks, TD-MS analyses were carried out. It was anticipated that the removal of guest molecules from **1** and **2** would allow these materials to exhibit gas occlusion properties. TD-MS data for **1** has already been presented in a previous paper.<sup>2d</sup>

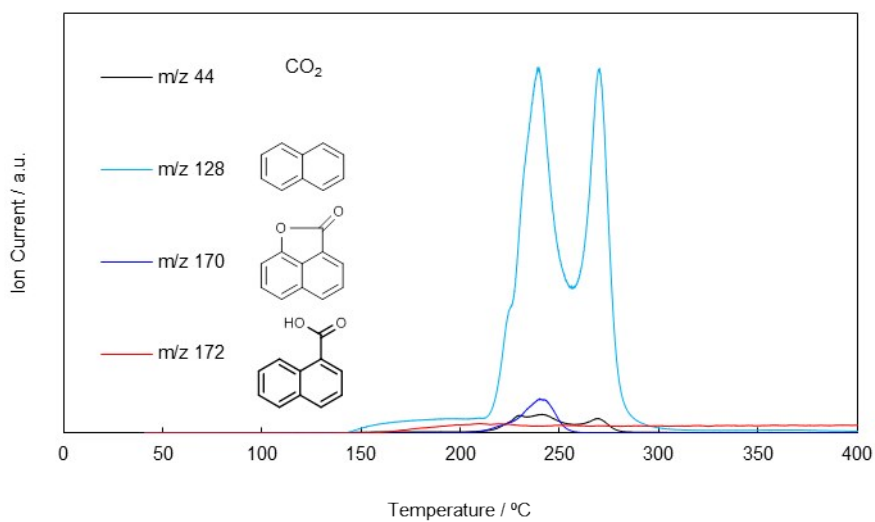


**Figure 2S.** TD-MS data for **2**.

#### 4. Synchrotron PXRD data for **1** and **2**.

*In situ* synchrotron PXRD ( $\lambda=0.24817 \text{ \AA}$ ) data were acquired under vacuum, 1 MPa  $\text{N}_2$  or 1 MPa  $\text{CO}_2$ . The resulting peaks obtained from **1** do not exhibit any shifts under vacuum, 1 MPa  $\text{N}_2$  or 1 MPa  $\text{CO}_2$  (Figure 3S-1). In contrast, the closed-open structural transformation of **2** was evident (Figure 4S-1). At 1 MPa  $\text{CO}_2$ , several of the peaks generated by **2** shift to lower angles compared to those obtained under vacuum or at 1 MPa  $\text{N}_2$ , indicating the expansion of the network upon  $\text{CO}_2$  adsorption.

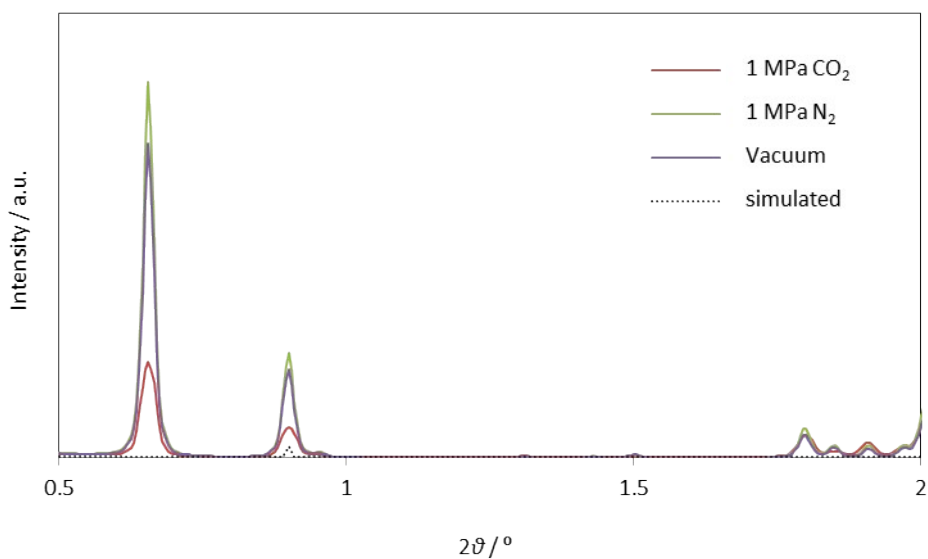


**Figure 3S-1.** No several peaks shift for **1** accompanying  $\text{CO}_2$  sorption contrast for under vacuum and 1 MPa  $\text{N}_2$ .

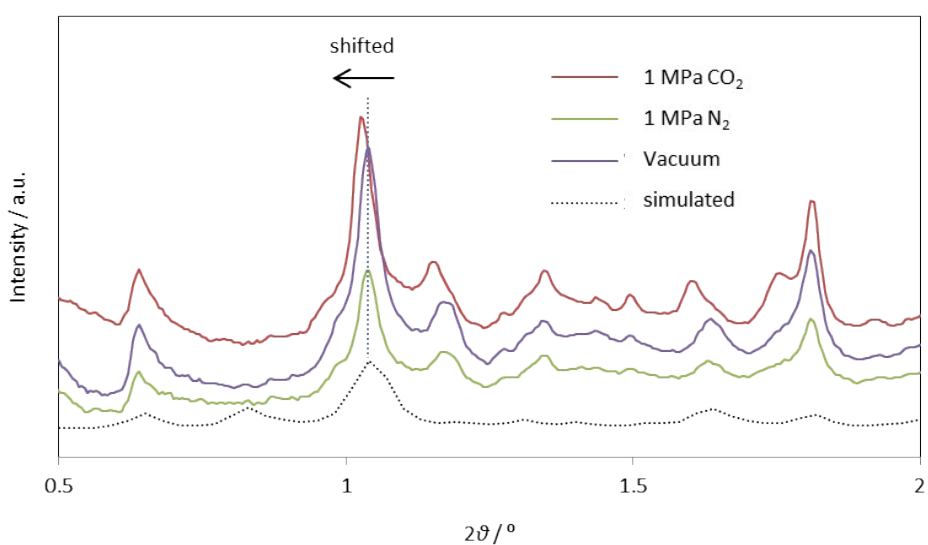


**Figure 3S-2.** Structural transformation of **2** accompanying  $\text{CO}_2$  sorption. The peaks at  $2\theta = 1.040^\circ$  under vacuum and  $1.025^\circ$  under 1 MPa  $\text{CO}_2$  correspond to the (1 2 0) plane, which is attributed to the layer gap.